DOI: 10.1002/ejic.201001145

Mixed-Metal d-f Phosphonate Frameworks – Photoluminescence and Magnetic Properties

João Rocha,*[a] Filipe A. Almeida Paz,*[a] Fa-Nian Shi,[a] Duarte Ananias,[a] Nuno J. O. Silva,[b] Luís D. Carlos,[b] and Tito Trindade[a]

Keywords: Metal–organic frameworks / Lanthanides / Iron / Photoluminescence / Magnetic properties

The synthesis and structural characterisation of a novel family of highly symmetric (rhombohedral crystal system) frameworks, incorporating d- and f-block elements formulated as $[LnFe^{III}Fe^{II}_6(Hpmida)_6]\cdot nH_2O$ [Ln = Nd^{3+} (**1**), Gd^{3+} (**2**), Tb^{3+} (**3**), Er^{3+} (**4**)] is reported. This is the second example of a family of porous mixed d-f MOFs containing high-spin Fe^{2+} centres. These materials were prepared from an eutectic mixture (1:1 molar ratio, choline chloride/malonic acid) with a small amount of added water and isolated directly in large amounts as single crystalline phases. The structural details were revealed by single-crystal X-ray diffraction, variable-temperature powder X-ray diffraction, thermogravimetry, vibrational and Mössbauer spectroscopy and electron microscopy (SEM and EDS). Networks are assembled by unusual $[Fe_2(Hpmida)_2]^{2-}$ dimeric units, which connect to each other and to the lanthanide centres to form a 3D porous framework. The empty voids of this framework accommodate charge-balancing Fe^{3+} cations and uncoordinated water molecules, which are readily released without structural collapse at temperatures below 250 °C. The photoluminescence and magnetic properties of the compounds were studied at ambient and low temperature.

Introduction

Metal–organic frameworks (MOFs) are one of the most active research areas in chemistry and materials science.[1] The concept behind their assembly lies in the use of organic molecules (linkers) possessing two or more coordinating-capable functional groups and metal centres (nodes) to promote the formation of highly organised polymeric compounds, typically forming 3D networks. Because the combination of linkers and nodes is, in essence, infinite the exponential growth of the field was initially motivated by the intriguing architectures obtained.[2] More recently, with the advent of novel frameworks exhibiting interesting properties with real potential for application,[3] research is increasingly focused on the design of functional materials for industry, particularly for gas adsorption,[4] heterogeneous catalysis,[5] fabrication of thin films or membranes,[6] sensors (e.g., ethanol and pH),[7] photoluminescence or magnetism[8] and MRI contrast agents[9] among others.

Traditionally, the functional groups of the organic linkers were mainly pyridine rings and carboxylate groups but, more recently, other moieties such as imidazole, sulfonates and phosphonate groups have been used. In particular, tetrahedral units are interesting anchoring sites to many types of metal centres, leading to MOFs with unusual architectures and potentially useful applications.[10] Indeed, three tetrahedrally arranged oxygen atoms emulate zeolite building blocks, allowing straightforward coordination to transition and lanthanide metal centres, and the presence of a carbon atom permits the inclusion of almost any organic group. Moreover, phosphonate groups exhibit high chemical and thermal robustness and are therefore a viable route to the formation of highly stable frameworks. Many examples of remarkable phosphonate-based frameworks have been reported: the Ni-STA-12 framework discovered by Miller and collaborators[11] exhibits permanent porosity and a remarkable uptake of CO_2 over methane at ambient temperature (ca. ten times larger); Evans and collaborators[12] prepared a chiral bisphosphonate molecule for the design of homochiral frameworks, which they used as heterogeneous catalysts in various organic transformations, such as cyanosilylation of aldehydes and ring opening of *meso*-carboxylic anhydrides; Plabst and Bein[10b] discovered a functional porous framework (based on a previously designed tetraphosphonic acid) for which the charge-balancing Na^+ cations could be exchanged only by monovalent cations, excluding di- and trivalent ones; the group of Yue[10e] developed a new organic ligand based on *S*-proline for the construction of homochiral frameworks, which exhibit selective sorption abilities of nitrogen, water and methanol, over ethanol.

[a] Department of Chemistry, CICECO, University of Aveiro, 3810-193 Aveiro, Portugal
Fax: +351-234-370084
E-mail: rocha@ua.pt
filipe.paz@ua.pt
[b] Department of Physics, CICECO, University of Aveiro, 3810-193 Aveiro, Portugal

Supporting information for this article is available on the WWW under http://dx.doi.org/10.1002/ejic.201001145.

We have been interested in the rational design and properties of functional MOFs,[13] in particular those containing one or more phosphonate groups in the organic building block(s).[14] Following our (i) previous work using the dimeric $[V_2O_2(pmida)_2]^{4-}$ unit [H_4pmida = *N*-(phosphonomethyl)iminodiacetic acid],[13b] (ii) interest in the development of novel synthetic approaches for the preparation of MOFs (viz. the newly-developed hydroionothermal synthesis)[14k] and (iii) recent work in which we successfully combined d- and f-cations with a bisphosphonate molecule to construct a highly porous, photoluminescent family of frameworks,[14a] we wish to describe a novel family of mixed d-f frameworks whose structure is resilient to the well known lanthanide contraction effect: $[LnFe^{III}Fe^{II}_6(Hpmida)_6]\cdot nH_2O$ [Ln = Nd^{3+} (**1**), Gd^{3+} (**2**), Tb^{3+} (**3**), Er^{3+} (**4**)]. In addition, to the best of our knowledge, this family of structures is the second example of a porous mixed d-f MOF containing high-spin Fe^{2+} centres to date.[15] These materials are highly symmetric (crystallising in the rhombohedral crystal system) and constructed from previously reported[16] anionic $[Fe_2(Hpmida)_2]^{2-}$ dimeric units connected to lanthanide centres (solely by the phosphonate groups) and to partially-occupied charge-balancing Fe^{3+} cations. The presence of both d- and f-cations promotes multifunctionality and a preliminary assessment has been carried out of the magnetic (for **2**) and photoluminescent (for **3**) properties.

Results and Discussion

Structural Studies

Synthesis and Crystal Morphology

Materials formulated as $[LnFe^{III}Fe^{II}_6(Hpmida)_6]\cdot nH_2O$ [Ln = Nd^{3+} (**1**), Gd^{3+} (**2**), Tb^{3+} (**3**), Er^{3+} (**4**)], on the basis of single-crystal X-ray diffraction (Table 3) and powder X-ray diffraction studies, were directly isolated from the contents of the autoclaves as large single crystals as depicted in Figure 1. These compounds were isolated using hydroionothermal synthesis[14k] recently developed in our laboratories, in which the solvent is a eutectic mixture of choline chloride and malonic acid (melting point 10 °C) with a small amount of distilled water. Attempts to isolate these materials using typical hydrothermal and ionothermal approaches systematically failed to lead to either single crystals or microcrystalline powders with identical structures to the compounds described herein. Phase purity and homogeneity of the bulk materials have been confirmed by powder X-ray diffraction investigations (Figure 2).

The existence of Fe^{3+} as a charge-balancing cation was unequivocally confirmed by Mössbauer spectroscopy. For example, data for **4** revealed the presence of both Fe^{2+} and Fe^{3+} in the material with a rate of occupancy of ca. 84% and 16%, respectively (Figure S1). Similar results were observed for the other members of the series. Furthermore, energy dispersive X-ray analysis (EDS) of the isolated crystals did not reveal the presence of additional charge-balancing cations (such as Na^+), and the EDS ratios are also in good agreement with the empirical formulae of the materials.

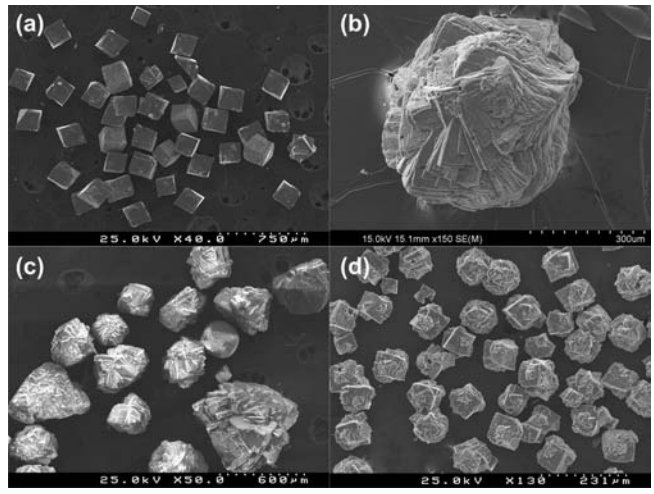

Figure 1. SEM pictures of crystals of $[LnFe^{III}Fe^{II}_6(Hpmida)_6]\cdot nH_2O$ [Ln = (a) Nd^{3+}, (b) Gd^{3+}, (c) Tb^{3+}, (d) Er^{3+}].

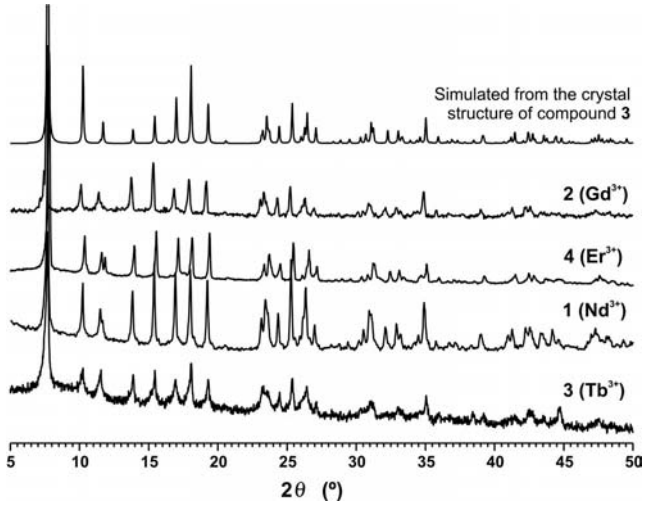

Figure 2. Comparison of the experimental powder X-ray diffraction patterns for $[LnFe^{III}Fe^{II}_6(Hpmida)_6]\cdot nH_2O$ [Ln = Nd^{3+} (**1**), Gd^{3+} (**2**), Tb^{3+} (**3**), Er^{3+} (**4**)] and a simulation based on the single-crystal structural determination of **3**, performed using the software package Mercury from the Cambridge Structural Database.[32]

Crystal Structure Description – Coordination Environments

The structural features of $[LnFe^{III}Fe^{II}_6(Hpmida)_6]\cdot nH_2O$ [Ln = Nd^{3+} (**1**), Gd^{3+} (**2**), Tb^{3+} (**3**), Er^{3+} (**4**)] have been revealed by single-crystal X-ray diffraction (Table 3). Because all structures are identical, the structural discussion outlined will focus on **3** with all features being valid for the other members of the series.

The framework of **3** is assembled from two metal centres, Tb(1) and Fe(1), with the third cation, Fe(2), half-occupied in its local crystallographic position. Because of charge-balancing reasons and in conjunction with data from Mössbauer spectroscopy, we assumed that this location was at-

tributed to the Fe^{3+} ion. We emphasise that this strategy arises from a simplification of the system to better understand the structural model and analyse the magnetic properties (vide infra). It is, however, also feasible to assume that the +2 and +3 charges for these cations could be distributed between the two crystallographic locations. Tb(1) is located at the threefold axis of the rhombohedral $R\bar{3}$ space group and is coordinated to six symmetry-related phosphonate groups. The coordination environment, $\{TbO_6\}$ (Figure 3a), resembles a slightly distorted octahedron in which the Tb–O bond lengths are identical [2.269(3) Å, Table 1], and the internal *cis* octahedral angles range from 88.93(11) to 91.07(11)° (Table 2).

As previously reported for complexes with V^{4+},[13b] the $Hpmida^{3-}$ anionic unit behaves as a multidentate chelating agent, effectively trapping the Fe^{2+} centre [Fe(1)] inside three five-membered chelating rings as depicted in Figure 3b. Two such chelates are linked to form the dimeric $[Fe_2(Hpmida)_2]^{2-}$ unit (vida infra). Hence, the coordination sphere of Fe(1) is composed of atoms arising from three symmetry-related $Hpmida^{3-}$ ligands, $\{FeNO_5\}$, with a geometry closely resembling a highly distorted octahedron. The Fe–(N,O) bond lengths range from 2.108(3) to 2.260(3) Å (Table 1 and Figure 3b), and the *cis* and *trans* internal octahedral angles are found in the range 77.08(12)–114.92(12)° and 158.63(11)–167.32(12)°, respectively. Notably, the extreme values for the bond lengths arise from the apical positions in the octahedron, which are those of the central N atom of $Hpmida^{3-}$ and the bridge to O(7) from a neighbouring dimeric $[Fe_2(Hpmida)_2]^{2-}$ unit.

Fe(2) appears in the crystal structure as a charge-balancing cation with a charge of +3 and is half occupied in its crystallographic position. Hence, because this cation seems to have a negligible importance in the construction of the framework it occupies an empty space between adjacent dimeric $[Fe_2(Hpmida)_2]^{2-}$ units with a highly distorted six-coordinate environment. It interacts more strongly with

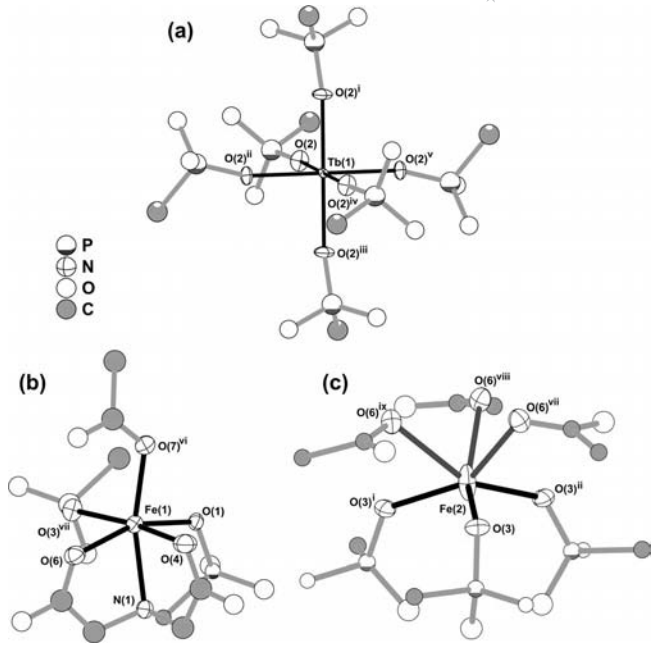

Figure 3. Schematic representation of the chemical environments of the metallic centres present in $[TbFe^{III}Fe^{II}_6(Hpmida)_6]\cdot nH_2O$ (**3**): (a) $\{TbO_6\}$, (b) $\{Fe^{II}NO_5\}$ and (c) $\{Fe^{III}O_6\}$. Thermal ellipsoids (for the atoms composing the coordination polyhedra) are represented at the 60% probability level. For selected bond lengths (Å) and angles (°) see Table 1 and Table 2, respectively. Symmetry transformations used to generate equivalent atoms: (i) 1 + *y*, –1 + *z*, *x*; (ii) *z*, –1 + *x*, 1 + *y*; (iii) –*y*, –*z*, 1 – *x*; (iv) 1 – *x*, –1 – *y*, 1 – *z*; (v) 1 – *z*, –*x*, –*y*; (vi) *y*, *z*, *x*; (vii) 1 – *x*, –*y*, 1 – *z*; (viii) 1 – *z*, –*x*, 1 – *y*; (ix) 1 – *y*, –*z*, 1 – *x*.

Table 1. Bond lengths (in Å) for the metallic coordination spheres present in $[LnFe^{III}Fe^{II}_6(Hpmida)_6]\cdot nH_2O$ [Ln = Nd^{3+} (**1**), Gd^{3+} (**2**), Tb^{3+} (**3**), Er^{3+} (**4**)].[a]

	1[b]	**2**[c]	**3**[d]	**4**[e]		**1**[b]	**2**[c]	**3**[d]	**4**[e]
Ln(1)–O(2)	2.330(2)	2.285(4)	2.269(3)	2.234(3)	Fe(1)–O(1)	2.116(2)	2.111(3)	2.117(3)	2.111(3)
Ln(1)–O(2)^{i}	2.330(2)	2.285(4)	2.269(3)	2.234(3)	Fe(1)–O(3)$^{x,\ vii,\ vii,\ vii}$	2.120(2)	2.131(4)	2.133(3)	2.125(3)
Ln(1)–O(2)^{ii}	2.330(2)	2.285(4)	2.269(3)	2.234(3)	Fe(1)–O(4)	2.206(3)	2.205(4)	2.200(3)	2.199(4)
Ln(1)–O(2)^{iii}	2.330(2)	2.285(4)	2.269(3)	2.234(3)	Fe(1)–O(6)	2.113(3)	2.118(4)	2.126(3)	2.128(3)
Ln(1)–O(2)^{iv}	2.330(2)	2.285(4)	2.269(3)	2.234(3)	Fe(1)–O(7)$^{ix,\ ix,\ vi,\ ix}$	2.112(3)	2.104(4)	2.108(3)	2.104(3)
Ln(1)–O(2)^{v}	2.330(2)	2.285(4)	2.269(3)	2.234(3)	Fe(1)–N(1)	2.260(3)	2.258(4)	2.260(3)	2.244(4)
					Fe(2)–O(3)$^{vi,\ vi,\ –,\ vi}$	2.299(2)	2.280(4)	2.296(3)	2.278(3)
					Fe(2)–O(3)$^{vii,\ viii,\ i,\ vii}$	2.299(2)	2.280(4)	2.296(3)	2.278(3)
					Fe(2)–O(3)$^{viii,\ vii,\ ii,\ viii}$	2.299(2)	2.280(4)	2.296(3)	2.278(3)
					Fe(2)–O(6)^{vii}	2.503(2)	2.514(4)	2.451(3)	2.446(3)
					Fe(2)–O(6)^{viii}	2.503(2)	2.514(4)	2.451(3)	2.446(3)
					Fe(2)–O(6)^{ix}	2.503(2)	2.514(4)	2.451(3)	2.446(3)

[a] Order of appearance of symmetry codes: one code or none, the same code for the four structures; four codes, order: 1, 2, 3, 4. [b] Symmetry transformations used to generate equivalent atoms for **1**: (i) –*y*, –*z*, 1 – *x*; (ii) 1 – *x*, –1 – *y*, 1 – *z*; (iii) *z*, –1 + *x*, 1 + *y*; (iv) 1 – *z*, –*x*, –*y*; (v) 1 + *y*, –1 – *z*, *x*; (vi) 1 + *y*, *z*, *x*; (vii) *x*, 1 + *y*, *z*; (viii) *z*, *x*, 1 + *y*; (ix) *y*, *z*, *x*; (*x*) 1 – *x*, –*y*, 1 – *z*. [c] Symmetry transformations used to generate equivalent atoms for **2**: (i) 1 – *z*, –*x*, –*y*; (ii) 1 + *y*, –1 + *y*, *x*; (iii) 1 – *x*, –1 – *y*, 1 – *z*; (iv) *z*, –1 + *x*, 1 + *y*; (v) –*y*, –*z*, 1 – *x*; (vi) 1 – *z*, 1 – *x*, –*y*; (vii) 1 – *x*, –*y*, 1 – *z*; (viii) –*y*, 1 – *z*, 1 – *x*; (ix) *y*, *z*, *x*. [d] Symmetry transformations used to generate equivalent atoms for **3**: (i) 1 + *y*, –1 + *z*, *x*; (ii) *z*, –1 + *x*, 1 + *y*; (iii) –*y*, –*z*, 1 – *x*; (iv) 1 – *x*, –1 – *y*, 1 – *z*; (v) 1 – *z*, –*x*, –*y*; (vi) *y*, *z*, *x*; (vii) 1 – *x*, –*y*, 1 – *z*; (viii) 1 – *z*, –*x*, 1– *y*; (ix) 1 – *y*, –*z*, 1 – *x*. [e] Symmetry transformations used to generate equivalent atoms for **4**: (i) *z*, –1 + *x*, 1 + *y*; (ii) 1 + *y*, –1 + *z*, *x*; (iii) 1 – *x*, –1 – *y*, 1 – *z*; (iv) –*y*, –*z*, 1 – *x*; (v) 1 – *z*, –*x*, –*y*; (vi) –*y*, 1 – *z*, 1 – *x*; (vii) 1 – *x*, –*y*, 1 – *z*; (viii) 1 – *z*, 1 – *x*, –*y*; (ix) *y*, *z*, *x*.

Table 2. Bond angles (°) for the Tb(1) and Fe(1) coordination environments present in **3**.[a]

$O(2)^{i}$ –Tb(1)–$O(2)^{ii}$	88.93(11)
$O(2)^{i}$–Tb(1)–$O(2)^{iii}$	180.0
$O(2)^{ii}$–Tb(1)–$O(2)^{iii}$	91.07(11)
$O(2)^{i}$–Tb(1)–$O(2)^{iv}$	91.07(11)
$O(2)^{ii}$–Tb(1)–$O(2)^{iv}$	91.07(11)
$O(2)^{iii}$–Tb(1)–$O(2)^{iv}$	88.93(11)
$O(2)^{i}$–Tb(1)–O(2)	88.93(11)
$O(2)^{ii}$–Tb(1)–O(2)	88.93(11)
$O(2)^{iii}$–Tb(1)–O(2)	91.07(11)
$O(2)^{iv}$–Tb(1)–O(2)	180.000(19)
$O(2)^{i}$–Tb(1)–$O(2)^{v}$	91.07(11)
$O(2)^{ii}$–Tb(1)–$O(2)^{v}$	180.000(19)
$O(2)^{iii}$–Tb(1)–$O(2)^{v}$	88.93(11)
$O(2)^{iv}$–Tb(1)–$O(2)^{v}$	88.93(11)
O(2)–Tb(1)–$O(2)^{v}$	91.07(11)
$O(7)^{vi}$–Fe(1)–O(1)	86.45(11)
$O(7)^{vi}$–Fe(1)–O(6)	114.92(12)
O(1)–Fe(1)–O(6)	158.63(11)
$O(7)^{vi}$–Fe(1)–$O(3)^{vii}$	89.83(12)
O(1)–Fe(1)–$O(3)^{vii}$	99.71(11)
O(6)–Fe(1)–$O(3)^{vii}$	81.51(12)
$O(7)^{vi}$–Fe(1)–O(4)	93.87(12)
O(1)–Fe(1)–O(4)	92.62(12)
O(6)–Fe(1)–O(4)	85.93(12)
$O(3)^{vii}$–Fe(1)–O(4)	167.32(12)
$O(7)^{vi}$–Fe(1)–N(1)	165.39(12)
O(1)–Fe(1)–N(1)	81.74(11)
O(6)–Fe(1)–N(1)	77.08(12)
$O(3)^{vii}$–Fe(1)–N(1)	100.58(12)
O(4)–Fe(1)–N(1)	78.18(12)

[a] Symmetry transformations used to generate equivalent atoms: (i) 1 + *y*, –1 + *z*, *x*; (ii) *z*, –1 + *x*, 1 + *y*; (iii) –*y*, –*z*, 1 – *x*; (iv) 1 – *x*, –1 – *y*, 1 – *z*; (v) 1 – *z*, –*x*, –*y*; (vi) *y*, *z*, *x*; (vii) 1 – *x*, –*y*, 1 – *z*.

three symmetry-related phosphonate groups [Fe–O distance of 2.296(3) Å], whereas the remaining three interactions (to three symmetry-related carboxylate moieties) are weaker [Fe–O distance of 2.451(3) Å, Figure 3c].

Crystal Structure Description: Secondary Building Unit

Residues of H_4pmida predictably self-assemble with V^{4+} into dimeric anionic $[V_2O_2(pmida)_2]^{4-}$ centrosymmetric units (Scheme 1 top).[14b–14f,17] Indeed, this predictability in the self-assembly process and the final robustness of the unit allowed us to design and construct several novel architectures.[13b] Because of the chelating fashion of the ligand and the presence of the terminal V=O oxido group, the connectivity of the $[V_2O_2(pmida)_2]^{4-}$ unit with other building blocks could only be achieved through the external oxygen atoms (from both the carboxylate and phosphonate moieties).[13b,17b] The $[LnFe^{III}Fe^{II}_6(Hpmida)_6]\cdot nH_2O$ [Ln = Nd^{3+} (**1**), Gd^{3+} (**2**), Tb^{3+} (**3**), Er^{3+} (**4**)] materials contain instead $[Fe_2(Hpmida)_2]^{2-}$ dimeric units (Scheme 1 bottom), which share remarkable resemblances with the V^{4+} unit. However, they contain Fe^{2+} centres which possess an unsaturated coordination sphere. This structural feature has remarkable consequences when this unit is used in the construction of multidimensional frameworks. This vacant coordination site permits the existence of direct connections between adjacent dimeric units, ultimately leading to the formation of extended structures such as coordination polymers with charge-balancing Na^+, K^+ and Rb^+ cations.[16]

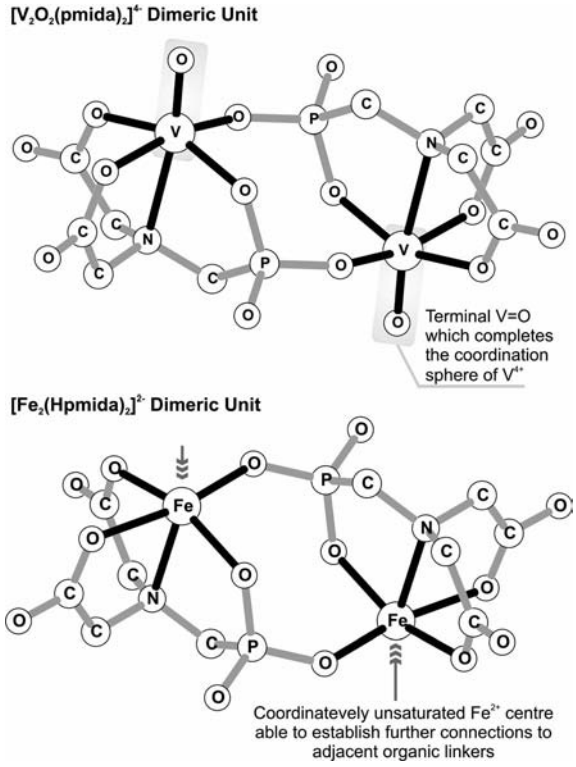

Scheme 1. Comparison of the anionic $[V_2O_2(pmida)_2]^{4-}$ and $[Fe_2(Hpmida)_2]^{2-}$ dimeric units. Black-filled bonds correspond to those comprising the coordination sphere of the metal centres.

Crystal Structure Description – Framework Construction

The vacant coordination sites in each $[Fe_2(Hpmida)_2]^{2-}$ dimeric unit (Scheme 1 bottom) also allow the formation of direct bridges among adjacent secondary building units. As depicted in Figure 4, one carboxylate group of the $Hpmida^{3-}$ ligand can establish a *syn*,*anti*-bridge between two adjacent dimeric units, with the connection occurring at the vacant coordination site of the Fe(1) metal centre, ultimately imposing an interunit/intermetallic Fe···Fe distance of 5.1751(8) Å. Because each dimeric unit possesses two such vacant coordination sites and binds through the two carboxylate groups, each unit is, thus, connected to another four (Figure 4 top centre), forming an Euclidian plane net whose tiling is composed of triangles and hexagons. The networks are related by threefold symmetry along the [111] direction of the unit cell, leading to close packing of the ABCABC··· type. Remarkably, connections between these adjacent networks formed by the anionic $[Fe_2(Hpmida)_2]^{2-}$ dimeric units are reinforced by the octahedral lanthanide centres (Figure 4 bottom right), which connect to the external phosphonate moieties. The overall framework is characterised by the presence of large empty voids which can contain uncoordinated water molecules and charge-balancing Fe^{3+} cations (Figure 4 bottom centre).

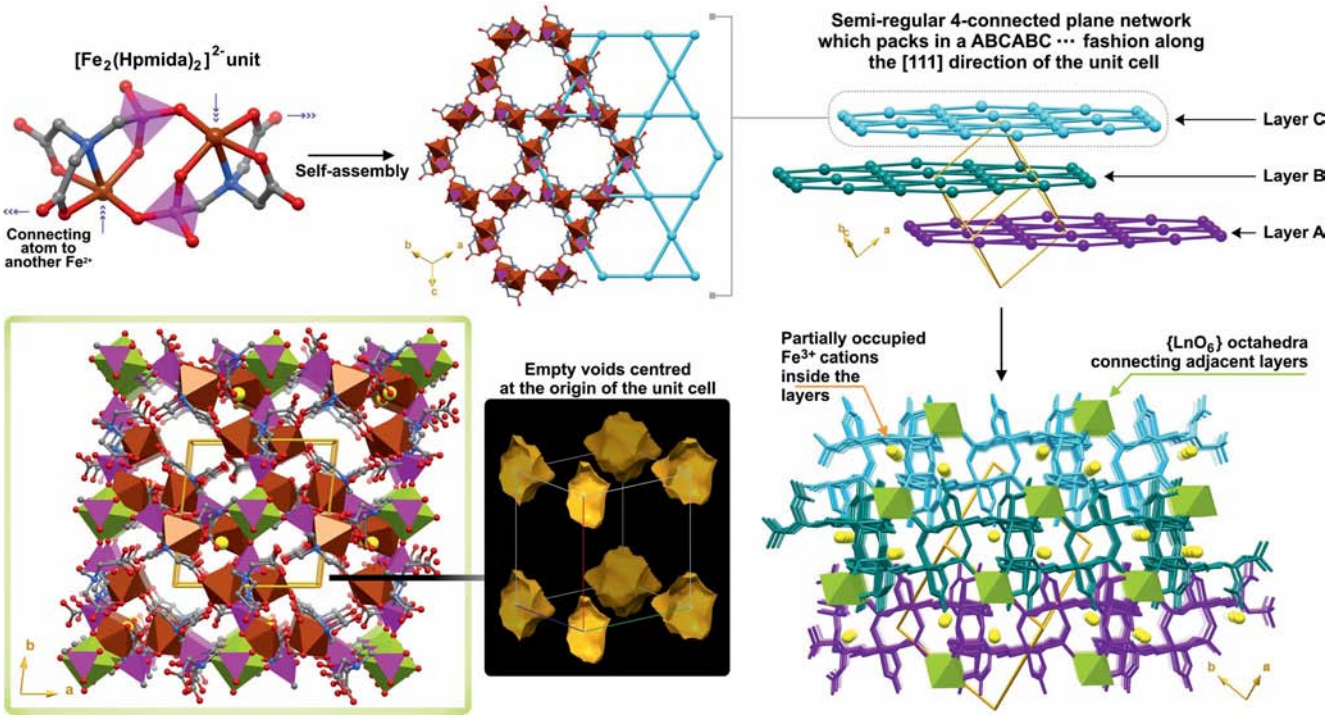

Figure 4. Schematic representation of the structural construction of $[LnFe^{III}Fe^{II}_6(Hpmida)_6]\cdot nH_2O$ [Ln = Nd^{3+} (**1**), Gd^{3+} (**2**), Tb^{3+} (**3**), Er^{3+} (**4**)]: adjacent dimeric $[Fe_2(Hpmida)_2]^{2-}$ anionic units possessing coordinatively unsaturated sites at the Fe^{2+} centres self-assemble into four-connected plane nets which are glued together by the octahedral lanthanide centres, leading to the formation of empty cages inside the structure. Charge-balancing Fe^{3+} centres (represented as yellow spheres) are partially occupied (50%) and structurally located nearby the dimeric anionic units. Voids have been calculated using Mercury from the Cambridge Structural Database,[32] by selecting a probe molecule with a radius of ca. 1.2 Å (such as water).

Vibrational Spectroscopy, Thermogravimetry and Variable-Temperature Powder X-ray Diffraction Studies

FTIR spectroscopic studies (Figure S2) produce very similar spectral features for all the materials prepared, clearly exhibiting the main diagnostic bands associated with the primary building blocks of **1**–**4**, in particular the presence of the $Hpmida^{3-}$ residues.[18] The existence of uncoordinated water molecules trapped inside the cavities and weakly bonded to the structure is evident from a broad band centred at ca. 3470 cm^{-1}, attributed to the typical υ(O–H) stretching vibrational mode, and by the presence of the in-plane deformation of water molecules [δ(H–O–H)] as a medium-to-strong intensity band at centred at about 1690 cm^{-1}. The coordination of the carboxylate and phosphonate groups to the central Fe^{2+} cations is also clearly visible, particularly in the 1700–1300 and 1150–1000 cm^{-1} regions, respectively. The typical symmetrical [$\upsilon_{sym}(PO_2)$] and asymmetrical [$\upsilon_{asym}(PO_2)$] stretching modes of the phosphonate groups appear as medium-to-strong vibrational bands. The antisymmetric and symmetric stretching bands arising from the carboxylate groups are present leading to a $\Delta[\nu_{asym}(CO_2^-) - \nu_{sym}(CO_2^-)]$ value calculated to be around 170 cm^{-1}, which agrees with the presence of carboxylate functional groups coordinated in a typical *anti*-unidentate coordination fashion as seen in the crystal structures.[19]

Thermogravimetric studies of **1**–**4** show that all compounds are thermally stable up to ca. 250 °C (Figure S3), followed by a considerable weight loss (ca. 26% for all structures) attributed to an initial framework destruction due to oxidation of the organic component. Indeed, in situ variable-temperature powder X-ray diffraction studies of **4** (Figure 5) reveal that the framework starts to collapse be-

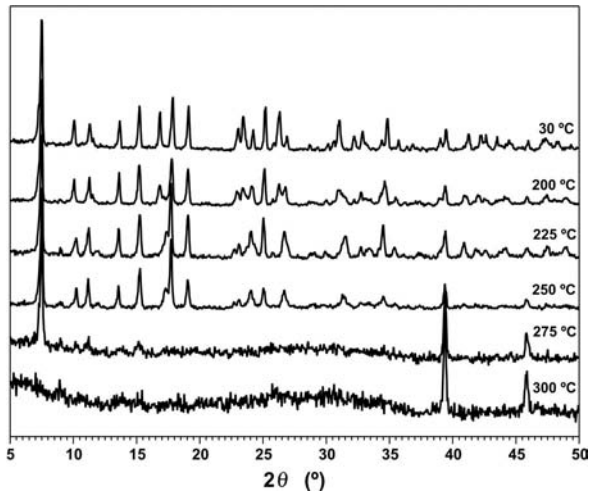

Figure 5. In situ variable-temperature powder X-ray diffraction study of **4** between ambient temperature and 300 °C.

tween 250–275 °C. The weight losses observed up to ca. 250 °C are attributed to the gradual release of the confined water molecules from the structure cavities.

Photoluminescence

The room temperature and 10 K excitation spectra of **3** (Figure 6) display a series of sharp Tb^{3+} lines ascribed to the intra-$4f^8$ transitions between the $^7F_6$ and $^5G_{1–6}$, $^5L_{10}$, $^5D_{1–4}$ levels, partially superimposed on a broad band in the range 300–420 nm (Figure 6 bottom; 10 K), monitored at 450 nm on the band attributed to the emission of the ligand. The temperature shift of the Tb^{3+} excitation spectra in this range could be attributed to the presence of a ligand-to-metal-charge-transfer (LMCT) process. The broad bands below 290 nm are assigned to the spin-allowed (low-spin, LS) and spin-forbidden (high-spin, HS) interconfigurational Tb^{3+} f–d transitions, respectively.[20]

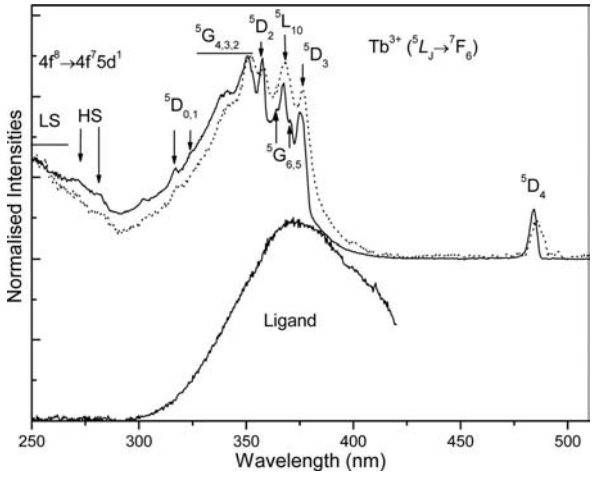

Figure 6. Excitation spectra of **3** monitored at 542 nm (upper spectra), recorded at 10 K (solid line) and at room temperature (dotted line). The excitation spectrum (bottom) was recorded at 10 K while monitoring the emission at 450 nm.

The room temperature and 10 K emission spectra of **3** excited at 351 nm (Figure 7) exhibit a series of sharp lines assigned to the $^5D_4 \rightarrow {}^7F_{1–6}$ transitions of Tb^{3+}. Photoluminescence from higher excited states (e.g. $^5D_3$) is not observed, indicating a very efficient nonradiative relaxation to the $^5D_4$ level. The spectra also display a broad blue band (peaking at ca. 425 nm) attributed to the emission from the ligand, which does not significantly overlap with the excitation spectrum of Tb^{3+}. Therefore an efficient LMCT process in **3** is not expected to occur. The integrated emission intensity, with excitation at 351 nm, increases by ca. three times with the decrease of temperature from 293 to 10 K (Figure 7) demonstrating a relevant influence of the nonradiative processes on the emission of **3** at room temperature. These nonradiative processes are even more effective in **1** and **4**, for which the typical infrared emissions are completely negligible at room temperature.

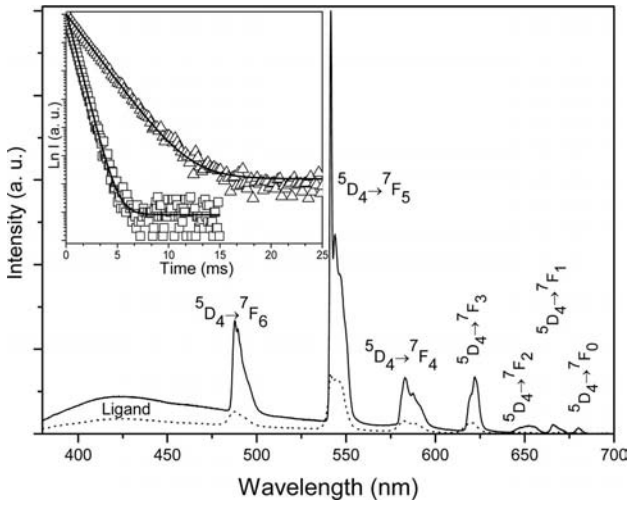

Figure 7. Emission spectra of **3** excited at 351 nm, recorded at 10 K (solid line) and at room temperature (dotted line). The spectrum inset shows the Tb^{3+} $^5D_4$ decay curves monitored at 542 nm under 229 nm excitation at 10 K (triangles) and at room temperature (squares). The solid lines are the best single exponential fit ($R > 0.999$) of the data sets.

The $^5D_4$ decay curves monitored at 542 nm ($^5D_4 \rightarrow {}^7F_5$ transition) and excited at 229 nm (Tb^{3+} LS f–d transition) can be fitted by monoexponential functions (inset in Figure 7), giving a lifetime of 0.72 ± 0.01 and 2.07 ± 0.01 ms at room temperature and 10 K, respectively, which supports the presence of a single local Tb^{3+} environment in good agreement with the crystallographic studies. This temperature dependence of the emission lifetime further supports the strong nonradiative mechanism of the Tb^{3+} emission at room temperature.

Magnetic Studies

For $T > 200$ K, χT of **2** is essentially constant after subtracting the diamagnetic contribution and equal to 25.8 cm^3 K/mol (Figure 8). This value is lower than that expected for a system composed of paramagnetic (isolated) ions (1 Gd^{3+} + 6 Fe^{2+}+ 1 Fe^{3+} per unit formula) considering the average χT experimentally found for Fe^{2+} and its lower bound value.[21] This is a clear evidence of the existence of antiferromagnetic (AF) coupling up to room temperature. The candidates for such coupling can be identified by the proposed structure. According to the structure, the most intense magnetic interactions are expected to appear in the tetranuclear cluster (C4) composed of three Fe^{2+} ions and one central Fe^{3+} ion (Figure 9). Yet, even if the contribution of C4 is zero, the paramagnetic contribution of the remaining ions (1 Gd^{3+} + 3 Fe^{2+} per unit formula) would still be larger than χT at low temperature, which implies the existence of further clusters with dominant AF interactions. Again, from the structural analysis, the candidate for having the AF interactions responsible for the decrease of χT compared to the isolated ions is the Fe^{2+} triangular cluster (C3).

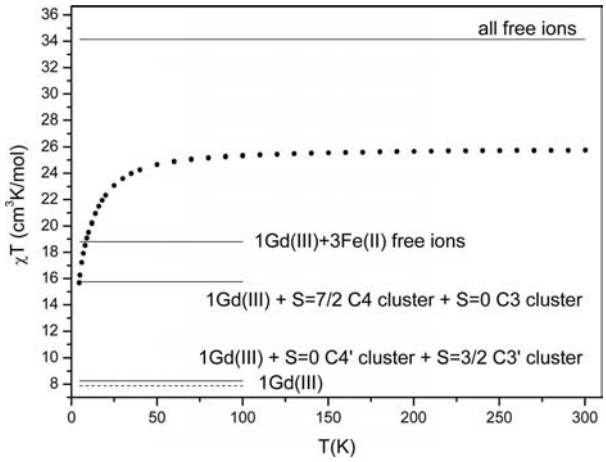

Figure 8. Temperature dependence of the susceptibility temperature product χT of **2**. Horizontal lines represent the ground state value of χT expected for different magnetic configurations.

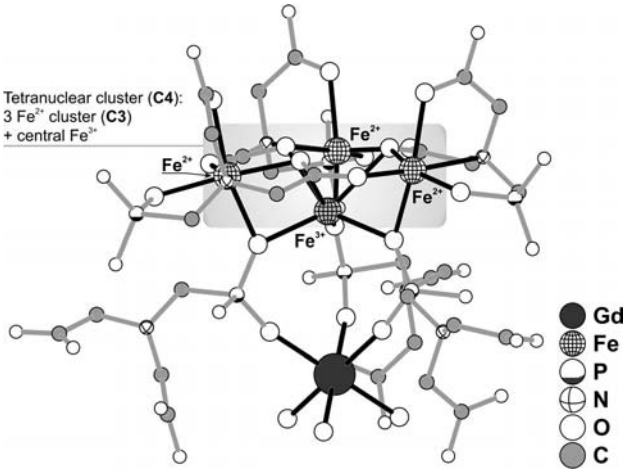

Figure 9. Schematic representation of a portion of the crystal structural model of **2** emphasising the Fe^{2+}/Fe^{3+} tetranuclear cluster (**C4**) in close proximity to the Gd^{3+} centre.

The relative energies of the states of C4 are given by $E(S,S') = -(J/2)[S(S + 1) - S'(S' + 1)]$,[22] where S is the total spin number and S' is the total spin of the three noncentral ions. In this case, for AF interactions, the ground state is $E(7/2,6)$, corresponding to three Fe^{2+} "up" and one Fe^{3+} "down". In the case of C3, the relative energies can be found in ref.[22] The ground state depends on the ratio between the different exchange coupling between the three magnetic centres; for the symmetric situation where the exchange coupling values are similar, the ground state corresponds to $S = 0$. Accordingly, the total contribution to the magnetic susceptibility at low temperature per unit formula is: one isolated Gd^{3+} ion, a tetranuclear cluster (C4) with ground state spin $S = 7/2$ and a trinuclear cluster (C3) with $S = 0$. These values give a total $\chi T = 15.76\ cm^3\ K/mol$, in agreement with the experimental low temperature value (Figure 8). As temperature increases, energy levels other than the ground state of the clusters become available, leading to the increase of χT.

We have considered that all Fe^{3+} ions are in C4, while in practice some or all Fe^{3+} can be in C3. In the case where all Fe^{3+} is in C3 (C3′) and C4 (C4′) is composed of Fe^{2+}, the ground state of C3′ is expected to be 3/2 while the ground state of C4′ is expected to be 0. Together with the Gd^{3+} ion, this corresponds to $\chi T = 9.754\ cm^3\ K/mol$, much lower than the experimental value (Figure 8). The system is most probably composed of a high fraction of C3 and C4 clusters, i.e., the Fe^{3+} ions are predominantly in the tetranuclear cluster.

Concluding Remarks

The use of a new hydroionothermal synthesis method (solvent: 1:1 molar ratio choline chloride/malonic acid eutectic mixture, with a small amount of water) led to a novel family of highly symmetric frameworks formulated as $[LnFe^{III}Fe^{II}_6(Hpmida)_6]\cdot nH_2O$ [Ln = Nd^{3+} (**1**), Gd^{3+} (**2**), Tb^{3+} (**3**), Er^{3+} (**4**)]. The frameworks are based on unusual $[Fe_2(Hpmida)_2]^{2-}$ dimeric units, which are mutually interconnected through the unsaturated Fe^{2+} centre to form Euclidian plane nets. The lanthanide centres coordinate preferentially to the phosphonate groups, gluing the aforementioned plane nets and leading to a 3D framework. Even though the structure easily releases the confined uncoordinated water molecules, the materials are thermally stable up to ca. 250 °C, as witnessed by TGA and variable-temperature powder X-ray diffraction.

The presence of d- and f-block elements promotes multifunctionality. Complex **3** is photoluminescent at ambient and low temperature, with the $^5D_4$ decay curves supporting the presence of a single local Tb^{3+} environment. Lowering the temperature considerably increases the emission of the material (by about three times) due to the reduction of the nonradiative processes, at the same time increasing the Tb^{3+} lifetime from 0.72 ± 0.01 to 2.07 ± 0.01 ms. The magnetic properties of this family of materials, in particular of **2**, are particularly sensitive to the local structural features: the presence of disordered, partially-occupied, charge-balancing Fe^{3+} cations has a strong impact on the overall magnetic behaviour of the compound because it leads to the formation of two different magnetic clusters.

It has been shown that the rational self-assembly of organic linkers with mixed functional groups (in particular phosphonate and carboxylate moieties) with d- and f-block elements may be used to engineer frameworks with specific properties. Indeed, the carboxylate groups of the H_4pmida residues are preferentially coordinated to the d-block elements whereas the lanthanides, due to their larger coordination sphere, prefer to coordinate to several phosphonate groups in a tetrahedral environment to reduce steric pressure. Moreover, these optical centres are free from coordinated water molecules, which often quench photoluminescence.

Experimental Section

Instrumentation

Sample morphology and identification of the main constituent elements (using EDS) were determined using a Low Vacuum Scanning Electron Microscope operating at 25 kV, FEG-SEM Hitachi S-4100, equipped with an energy dispersive X-ray analysis Römteck System and polymeric window. Samples were fixed in aluminium holders using adhesive carbon foil and were carbon-coated for analysis in the electron beam. FTIR spectra were collected from KBr pellets (Aldrich, 99%+, FTIR grade) with a Mattson 7000 FTIR spectrometer. Thermogravimetric analyses were carried out in air using a Shimadzu TGA-50, with a heating rate of 10 °C/min and a flow rate of 20 cm^3/min.

Conventional powder X-ray diffraction data for the materials were collected at ambient temperature with an X'Pert MPD Philips diffractometer (Cu-$K_{\alpha1,2}$ X-radiation, λ_1 = 1.540598 Å and λ_2 = 1.544426 Å), equipped with an X'Celerator detector and a flat-plate sample holder in a Bragg–Brentano para-focusing optics configuration (40 kV, 50 mA). Intensity data were collected by the step-counting method (step 0.02°), in continuous mode, in the ca. $5 \leq 2\theta \leq 50°$ range.

In situ variable-temperature powder X-ray diffraction data for **4** were collected with an X'Pert MPD Philips diffractometer (Cu-K_α X-radiation, λ = 1.54060 Å), equipped with an X'Celerator detector, a curved graphite-monochromated radiation, a flat-plate sample holder in a Bragg–Brentano para-focusing optics configuration (40 kV, 50 mA), and a high-temperature Anton Paar HKL 16 chamber, controlled by an Anton Paar 100 TCU unit. Intensity data were collected in the step mode (0.05°, 1 s per step) in the range ca. $5 \leq 2\theta° \leq 50$.

Reagents: Chemicals were readily available from commercial sources and were used as received without further purification: lanthanide(III) chloride hydrates ($LnCl_3 \cdot xH_2O$, Ln^{3+} = Nd^{3+}, Gd^{3+}, Tb^{3+} and Er^{3+}; of at least 99.9% purity, Sigma–Aldrich); *N*-(phosphonomethyl)iminodiacetic acid (H_4pmida, $C_5H_{10}NO_7P$, ≥97%, Fluka), $FeC_2O_4 \cdot 2H_2O$ (99%, Aldrich), choline chloride (≥98%, Aldrich) and malonic acid (≥99%, Aldrich).

Hydroionothermal Synthesis of $[LnFe^{III}Fe^{II}_6(Hpmida)_6] \cdot nH_2O$

A eutectic mixture (ionic liquid) was prepared by heating a mixture of choline chloride and malonic acid (CM) in a 1:1 mol ratio to 80 °C with constant magnetic stirring until a homogeneous transparent colourless liquid was formed.

To a mixture containing H_4pmida (0.38 g), $FeC_2O_4 \cdot 2H_2O$ (0.13 g) and $NdCl_3 \cdot 6H_2O$ (0.10 g) [or $GdCl_3 \cdot 6H_2O$ (0.10 g) or $TbCl_3 \cdot 6H_2O$ (0.15 g) or $ErCl_3 \cdot 6H_2O$ (0.15 g), molar ratios of approximately 6:2:1], were added CM (3.0 g) and an aqueous solution of NaOH (0.5–1.0 g, 10% in mass). The suspension was magnetically stirred for 1 h at ambient temperature in order to prepare a homogeneous gel, which was transferred to a 45 mL reaction vessel and placed inside a preheated oven at 150 °C. Reactions took place over a period of 90 h, after which time crystals of the desired products could be readily isolated from the amorphous gel-like bulk powder. Compounds were washed three times with ethanol (ca. 50 mL) with ultrasonic vibration, and distilled water (50 mL) and air dried at ambient temperature. Yields (based on $FeC_2O_4 \cdot 2H_2O$): 61% (**1**), 51% (**2**), 46% (**3**) and 76% (**4**).

Single-Crystal X-ray Diffraction

Single crystals of $[LnFe^{III}Fe^{II}_6(Hpmida)_6] \cdot nH_2O$ [where Ln^{3+} = Nd^{3+} (**1**), Gd^{3+} (**2**), Tb^{3+} (**3**) and Er^{3+} (**4**)] were manually harvested from crystallisation vials and mounted on Hampton Research CryoLoops using FOMBLIN Y perfluoropolyether vacuum oil (LVAC 25/6, purchased from Aldrich)[23] with the help of a Stemi 2000 stereomicroscope equipped with Carl Zeiss lenses. Data were collected with a Bruker X8 Kappa APEX II charge-coupled device (CCD) area-detector diffractometer (Mo-K_α graphite-monochromated radiation, λ = 0.71073 Å) controlled by the APEX2 software package,[24] and equipped with an Oxford Cryosystems Series 700 cryostream monitored remotely using Cryopad.[25] Images were processed using SAINT+,[26] and data were corrected for absorption by the multiscan semiempirical method implemented in SADABS.[27] Structures were solved using the Patterson synthesis algorithm implemented in SHELXS-97,[28] which allowed the immediate location of the heaviest atoms (namely the lanthanide centres and Fe). All remaining non-hydrogen atoms were located in difference Fourier maps calculated from successive full-matrix least-squares refinement cycles on F^2 using SHELXL-97.[28b,29] Non-hydrogen atoms were successfully refined using anisotropic displacement parameters.

The second site for iron, Fe(2), assumed to be the charge-balancing Fe^{3+} centre, was directly located from difference Fourier maps and was included in the final structural model with a fixed rate of occupancy of 50%, in agreement with both an unrestrained refinement of the site occupancy (which converged to roughly this value in all four crystallographic determinations) and Mössbauer data for **4**.

During crystal refinement using the original integrated and scaled data sets, it was clearly visible from difference Fourier maps that the voids present in the three structures most likely contain highly disordered solvent molecules. Nevertheless, the disorder associated with these chemical entities ultimately leads to a considerable smearing of the electron density, which prevented their location from difference Fourier maps. Attempts to include these chemical moieties using a battery of crystallographic constraints proved to be highly unfruitful, particularly due to the fact that the observed electron density was located surrounding special positions in the crystal structures. The original data sets were then treated using the SQUEEZE[30] subroutines provided with the software package PLATON[31] in order to eliminate from the overall electron density the contribution of the highly disordered solvent molecules present in the solvent-accessible area. PLATON estimated that, for 1 to 4, the respective unit cells contain ca. 265, 261, 260 and 251 Å3 of potential solvent accessible area (ca. 17.0, 17.0, 16.9 and 16.6% of the total volumes), in one large cavity centred at the origin of the unit cell. The resulting solvent-free reflection files produced by PLATON were used in subsequent refinement cycles using full-matrix least-squares on F^2 in SHELXL-97, leading to the crystallographic data summarised in Table 3.

The last difference Fourier map synthesis showed for **1** the highest peak (1.921 e $Å^{-3}$) and deepest hole (–1.207 e $Å^{-3}$) located at 0.66 and 0.88 Å from Nd(1), respectively; for **2** the highest peak (1.629 e $Å^{-3}$) and deepest hole (–3.857 e $Å^{-3}$) were located at 0.31 and 0.44 Å from Fe(1) and Gd(1), respectively; for **3** the highest peak (1.721 e $Å^{-3}$) and deepest hole (–1.486 e $Å^{-3}$) were located at 0.58 and 0.44 Å from Tb(1) and Fe(1), respectively; for **4** the highest peak (0.839 e $Å^{-3}$) and deepest hole (–0.896 e $Å^{-3}$) were located at 0.35 and 0.42 Å from Er(1) and Fe(1), respectively.

Crystallographic data (excluding structure factors) for the structures reported in this paper have been deposited with the Cambridge Crystallographic Data Centre (see deposition numbers in Table 3). These data can be obtained free of charge from The Cambridge Crystallographic Data Centre via www.ccdc.cam.ac.uk/data_request/cif.

Table 3. Crystal and structure refinement data for $[LnFe^{III}Fe^{II}_6(Hpmida)_6]\cdot nH_2O$ [Ln = Nd^{3+} (**1**), Gd^{3+} (**2**), Tb^{3+} (**3**), and Er^{3+} (**4**)] (data sets treated with SQUEEZE).

	1	**2**	**3**	**4**
Formula	$C_{30}H_{42}Fe_7N_6NdO_{42}P_6$	$C_{30}H_{42}Fe_7GdN_6O_{42}P_6$	$C_{30}H_{42}Fe_7N_6O_{42}P_6Tb$	$C_{30}H_{42}ErFe_7N_6O_{42}P_6$
Formula weight	1879.71	1892.72	1894.39	1902.73
Temperature [K]	100(2)	150(2)	150(2)	150(2)
Crystal system	Rhombohedral	Rhombohedral	Rhombohedral	Rhombohedral
Space group	$R\bar{3}$	$R\bar{3}$	$R\bar{3}$	$R\bar{3}$
a [Å]	11.6999(4)	11.6640(5)	11.6476(3)	11.5890(2)
b [Å]	11.6999(4)	11.6640(5)	11.6476(3)	11.5890(2)
c [Å]	11.6999(4)	11.6640(5)	11.6476(3)	11.5890(2)
α [°]	82.4010(10)	82.316(1)	82.470(1)	82.6630(10)
β [°]	82.4010(10)	82.316(1)	82.470(1)	82.6630(10)
γ [°]	82.4010(10)	82.316(1)	82.470(1)	82.6630(10)
Volume [Å^3]	1562.80(9)	1547.6(27)	1542.60(7)	1521.23(5)
Z	1	1	1	1
D_c [g cm^{-3}]	1.997	2.031	2.039	2.077
μ(Mo-K_α) [mm^{-1}]	2.652	2.911	2.991	3.250
F(000)	932	936	937	940
Crystal size [mm]	0.10 × 0.04 × 0.03	0.07 × 0.03 × 0.02	0.10 × 0.05 × 0.03	0.08 × 0.04 × 0.04
Crystal type	Colourless prisms	Brown prisms	Colourless prisms	Colourless prisms
θ range	3.54 to 29.13	3.55 to 36.31	3.55 to 30.51	3.57 to 25.33
Index ranges	$-16 \le h \le 16$	$-13 \le h \le 19$	$-16 \le h \le 15$	$-13 \le h \le 13$
	$-13 \le k \le 14$	$-19 \le k \le 13$	$-16 \le k \le 12$	$-13 \le k \le 13$
	$-15 \le l \le 15$	$-19 \le l \le 19$	$-16 \le l \le 13$	$-12 \le l \le 13$
Reflections collected	18428	17217	18844	31878
Independent reflections	2780 (R_{int} = 0.0530)	4976 (R_{int} = 0.0934)	3111 (R_{int} = 0.0435)	1846 (R_{int} = 0.0460)
Data completeness	to θ = 29.13°	to θ = 36.31°	to θ = 30.51°	to θ = 25.33°
	99.3%	99.0%	99.0%	99.6%
Final R indices [$I > 2\sigma(I)$][a,b]	$R1$ = 0.0367	$R1$ = 0.0648	$R1$ = 0.0387	$R1$ = 0.0299
	$wR2$ = 0.0995	$wR2$ = 0.1852	$wR2$ = 0.0973	$wR2$ = 0.0768
Final R indices (all data)[a,b]	$R1$ = 0.0480	$R1$ = 0.1107	$R1$ = 0.0550	$R1$ = 0.0348
	$wR2$ = 0.1055	$wR2$ = 0.2078	$wR2$ = 0.1027	$wR2$ = 0.0785
Weighting scheme[c]	m = 0.0602	m = 0.1020	m = 0.0412	m = 0.0307
	n = 1.2868	n = 0	n = 6.4239	n = 8.0391
Largest diff. peak and hole	1.921 and –1.207 e Å^{-3}	1.629 and –3.857 e Å^{-3}	1.721 and –1.486 e Å^{-3}	0.839 and –0.896 e Å^{-3}
CCDC deposition number	790983	798118	790984	790985

[a] $R1 = \sum \| F_o | - | F_c \| / \sum | F_o |$; [b] $wR2 = \sqrt{\sum \left[w\left(F_o^2 - F_c^2\right)^2 \right] / \sum \left[w\left(F_o^2\right)^2 \right]}$

[c] $w = 1/\left[\sigma^2\left(F_o^2\right) + \left(mP\right)^2 + nP \right]$ where $P = \left(F_o^2 + 2F_c^2\right)/3$

Photoluminescence: Photoluminescence measurements were recorded with a Fluorolog®-3 model FL3–2T with double excitation spectrometer (Triax 320), fitted with a 1200 grooves/mm grating blazed at 330 nm, and a single emission spectrometer (Triax 320), fitted with a 1200 grooves/mm grating blazed at 500 nm, coupled to a R928 photomultiplier. Excitation spectra were corrected from 240 to 600 nm for the spectral distribution of the lamp intensity using a photodiode reference detector. Emission spectra were also corrected for the spectral response of the monochromators and the detector using typical correction spectra provided by the manufacturer. Time-resolved measurements were carried out using a 1934D3 phosphorimeter coupled to a Fluorolog®-3 and a Xe-Hg flash lamp (6 μs/pulse half width and 20–30 μs tail) was used as excitation source. The measurements at 10 K were performed using a He closed-cycle cryostat.

Magnetic Studies: The magnetic susceptibility, χ, of **2** was recorded at increasing temperatures (up to 300 K) after an initial cooling from r.t. down to 2 K in the absence of the field (ZFC procedure), and cooling from 300 K down to 1.8 K at the measuring field (100 Oe). Measurements were performed with a SQUID magnetometer (Quantum Design, model MPMS-5s).

Supporting Information (see footnote on the first page of this article): Additional crystallographic tables summarising the bond angles of compounds **1**, **2** and **4**, Mössbauer spectrum of compound **4**, FTIR spectra and thermograms of all compounds.

Acknowledgments

We are grateful to Fundação para a Ciência e a Tecnologia (Portugal) for their financial support through the project PTDC/QUI-QUI/098098/2008 (FCOMP-01-0124-FEDER-010785), for specific funding toward the purchase of the single-crystal X-ray diffractometer and for the Ciencia2008 programme.

[1] a) N. R. Champness in *Making Crystals by Design – Methods, Techniques and Applications*, 1st ed. (Eds.: D. Braga, F. Grepioni), Wiley-VCH Verlag GmbH & Co. KGaA, Weinheim, **2007**, pp. 193–208; b) C. Janiak, *Dalton Trans.* **2003**, 2781–2804; c) B. Moulton, M. J. Zaworotko, *Chem. Rev.* **2001**, *101*, 1629–1658; d) G. S. Papaefstathiou, L. R. MacGillivray, *Coord. Chem. Rev.* **2003**, *246*, 169–184.

[2] a) S. R. Batten, R. Robson, *Angew. Chem. Int. Ed.* **1998**, *37*, 1461–1494; b) M. Eddaoudi, D. B. Moler, H. L. Li, B. L. Chen, T. M. Reineke, M. O'Keeffe, O. M. Yaghi, *Acc. Chem. Res.* **2001**, *34*, 319–330; c) L. Carlucci, G. Ciani, D. M. Proserpio, *Coord. Chem. Rev.* **2003**, *246*, 247–289; d) L. Carlucci, G. Ciani, D. M. Proserpio, *Crystengcomm* **2003**, *5*, 269–279.
[3] U. Mueller, M. Schubert, F. Teich, H. Puetter, K. Schierle-Arndt, J. Pastre, *J. Mater. Chem.* **2005**, *16*, 626–636.
[4] a) N. Nijem, J. F. Veyan, L. Z. Kong, K. H. Li, S. Pramanik, Y. G. Zhao, J. Li, D. Langreth, Y. J. Chabal, *J. Am. Chem. Soc.* **2010**, *132*, 1654–1664; b) Y. Yan, I. Telepeni, S. H. Yang, X. Lin, W. Kockelmann, A. Dailly, A. J. Blake, W. Lewis, G. S. Walker, D. R. Allan, S. A. Barnett, N. R. Champness, M. Schroder, *J. Am. Chem. Soc.* **2010**, *132*, 4092–4094; c) Y. S. Bae, K. L. Mulfort, H. Frost, P. Ryan, S. Punnathanam, L. J. Broadbelt, J. T. Hupp, R. Q. Snurr, *Langmuir* **2008**, *24*, 8592–8598; d) M. Dinca, A. Dailly, Y. Liu, C. M. Brown, D. A. Neumann, J. R. Long, *J. Am. Chem. Soc.* **2006**, *128*, 16876–16883; e) M. Dinca, J. R. Long, *J. Am. Chem. Soc.* **2005**, *127*, 9376–9377; f) L. J. Murray, M. Dinca, J. R. Long, *Chem. Soc. Rev.* **2009**, *38*, 1294–1314.
[5] a) J. Lee, O. K. Farha, J. Roberts, K. A. Scheidt, S. T. Nguyen, J. T. Hupp, *Chem. Soc. Rev.* **2009**, *38*, 1450–1459; b) L. Q. Ma, C. Abney, W. B. Lin, *Chem. Soc. Rev.* **2009**, *38*, 1248–1256.
[6] a) Y. S. Li, F. Y. Liang, H. Bux, A. Feldhoff, W. S. Yang, J. Caro, *Angew. Chem. Int. Ed.* **2010**, *49*, 548–551; b) X. Q. Zou, G. S. Zhu, F. Zhang, M. Y. Guo, S. L. Qiu, *CrystEngComm* **2010**, *12*, 352–354.
[7] a) B. V. Harbuzaru, A. Corma, F. Rey, P. Atienzar, J. L. Jorda, H. Garcia, D. Ananias, L. D. Carlos, J. Rocha, *Angew. Chem. Int. Ed.* **2008**, *47*, 1080–1083; b) B. V. Harbuzaru, A. Corma, F. Rey, J. L. Jorda, D. Ananias, L. D. Carlos, J. Rocha, *Angew. Chem. Int. Ed.* **2009**, *48*, 6476–6479.
[8] a) M. D. Allendorf, C. A. Bauer, R. K. Bhakta, R. J. T. Houk, *Chem. Soc. Rev.* **2009**, *38*, 1330–1352; b) K. Liu, H. P. You, Y. H. Zheng, G. Jia, Y. H. Song, Y. J. Huang, M. Yang, J. J. Jia, N. Guo, H. J. Zhang, *J. Mater. Chem.* **2010**, *20*, 3272–3279; c) Q. L. Zhu, T. L. Sheng, R. B. Fu, S. M. Hu, J. S. Chen, S. C. Xiang, C. J. Shen, X. T. Wu, *Cryst. Growth Des.* **2009**, *9*, 5128–5134; d) M. Kurmoo, *Chem. Soc. Rev.* **2009**, *38*, 1353–1379.
[9] G. A. Pereira, J. A. Peters, F. A. A. Paz, J. Rocha, C. Geraldes, *Inorg. Chem.* **2010**, *49*, 2969–2974.
[10] a) M. Plabst, T. Bein, *Inorg. Chem.* **2009**, *48*, 4331–4341; b) M. Plabst, L. B. McCusker, T. Bein, *J. Am. Chem. Soc.* **2009**, *131*, 18112–18118; c) G. K. H. Shimizu, R. Vaidhyanathan, J. M. Taylor, *Chem. Soc. Rev.* **2009**, *38*, 1430–1449; d) S. F. Tang, J. L. Song, X. L. Li, J. G. Mao, *Cryst. Growth Des.* **2006**, *6*, 2322–2326; e) Q. Yue, J. Yang, G. H. Li, G. D. Li, J. S. Chen, *Inorg. Chem.* **2006**, *45*, 4431–4439; f) A. Clearfield, *Curr. Opin. Solid State Mater. Sci.* **1996**, *1*, 268–278.
[11] S. R. Miller, G. M. Pearce, P. A. Wright, F. Bonino, S. Chavan, S. Bordiga, I. Margiolaki, N. Guillou, G. Feerey, S. Bourrelly, P. L. Llewellyn, *J. Am. Chem. Soc.* **2008**, *130*, 15967–15981.
[12] O. R. Evans, H. L. Ngo, W. B. Lin, *J. Am. Chem. Soc.* **2001**, *123*, 10395–10396.
[13] a) F. A. A. Paz, J. Klinowski, *Pure Appl. Chem.* **2007**, *79*, 1097–1110; b) F. A. A. Paz, J. Rocha, J. Klinowski, T. Trindade, F. N. Shi, L. Mafra, *Prog. Solid State Chem.* **2005**, *33*, 113–125.
[14] a) J. Rocha, F. A. A. Paz, F. N. Shi, R. A. S. Ferreira, T. Trindade, L. D. Carlos, *Eur. J. Inorg. Chem.* **2009**, 4931–4945; b) L. Cunha-Silva, F. N. Shi, J. Klinowski, T. Trindade, J. Rocha, F. A. A. Paz, *Acta Crystallogr., Sect. E.-Struct Rep. Online* **2008**, *64*, M39–M40; c) L. Cunha-Silva, F. N. Shi, J. Klinowski, T. Trindade, J. Rocha, F. A. A. Paz, *Acta Crystallogr., Sect. E.-Struct Rep. Online* **2007**, *63*, M372–M375; d) F. N. Shi, F. A. A. Paz, P. I. Girginova, V. S. Amaral, J. Rocha, J. Klinowski, T. Trindade, *Inorg. Chim. Acta* **2006**, *359*, 1147–1158; e) F. A. A. Paz, F. N. Shi, L. S. Mafra, A. Makal, K. Wozniak, T. Trindade, J. Klinowski, J. Rocha, *Acta Crystallogr., Sect. E.-Struct Rep. Online* **2005**, *61*, M1628–M1632; f) F. A. A. Paz, F. N. Shi, J. Klinowski, J. Rocha, T. Trindade, *Eur. J. Inorg. Chem.* **2004**, 2759–2768; g) L. Cunha-Silva, L. Mafra, D. Ananias, L. D. Carlos, J. Rocha, F. A. A. Paz, *Chem. Mater.* **2007**, *19*, 3527–3538; h) L. Cunha-Silva, D. Ananias, L. D. Carlos, F. A. A. Paz, J. Rocha, *Z. Kristallogr.* **2009**, *224*, 261–272; i) L. Cunha-Silva, S. Lima, D. Ananias, P. Silva, L. Mafra, L. D. Carlos, M. Pillinger, A. A. Valente, F. A. A. Paz, J. Rocha, *J. Mater. Chem.* **2009**, *19*, 2618–2632; j) F. N. Shi, L. Cunha-Silva, R. A. S. Ferreira, L. Mafra, T. Trindade, L. D. Carlos, F. A. A. Paz, J. Rocha, *J. Am. Chem. Soc.* **2008**, *130*, 150–167; k) F. N. Shi, T. Trindade, J. Rocha, F. A. A. Paz, *Cryst. Growth Des.* **2008**, *8*, 3917–3920.
[15] B. Zhao, X. Y. Chen, Z. Chen, W. Shi, P. Cheng, S. P. Yan, D. Z. Liao, *Chem. Commun.* **2009**, 3113–3115.
[16] D. Cave, F. C. Coomer, E. Molinos, H. H. Klauss, P. T. Wood, *Angew. Chem. Int. Ed.* **2006**, *45*, 803–806.
[17] a) Y. Q. Gao, W. Gu, X. P. Sun, X. Liu, D. Z. Liao, *Z. Anorg. Allg. Chem.* **2008**, *634*, 1961–1964; b) D. C. Crans, F. L. Jiang, O. P. Anderson, S. M. Miller, *Inorg. Chem.* **1998**, *37*, 6645–6655.
[18] G. Socrates, *Infrared Characteristic Group Frequencies - Tables and Charts*, 2nd ed., John Wiley & Sons Ltd, Baffins Lane, Chichester, **1994**.
[19] a) G. B. Deacon, R. J. Phillips, *Coord. Chem. Rev.* **1980**, *33*, 227–250; b) C. Oldham in *Comprehensive Coordination Chemistry*, vol. 2, 1st ed. (Ed.: S. G. Wilkinson), Pergamon Press, **1987**, pp. 435–459.
[20] L. van Pieterson, M. F. Reid, G. W. Burdick, A. Meijerink, *Phys. Rev. B* **2002**, *65*, 045114.
[21] R. L. Carlin, *Magnetochemistry*, Springer-Verlag, Berlin, **1986**.
[22] O. Kahn in *Molecular Magnetism*, Wiley-VCH, Weinheim, **1993**, ch. 10.
[23] T. Kottke, D. Stalke, *J. Appl. Crystallogr.* **1993**, *26*, 615–619.
[24] APEX2, *Data Collection Software Version 2.1-RC13, Bruker AXS, Delft, The Netherlands* **2006**.
[25] Cryopad, *Remote monitoring and control, Version 1.451, Oxford Cryosystems, Oxford, United Kingdom* **2006**.
[26] SAINT + , *Data Integration Engine v. 7.23a* © **1997–2005**, *Bruker AXS, Madison, Wisconsin, USA*.
[27] G. M. Sheldrick, *SADABS v.2.01, Bruker/Siemens Area Detector Absorption Correction Program* **1998**, *Bruker AXS, Madison, Wisconsin, USA*.
[28] a) G. M. Sheldrick, *SHELXS-97, Program for Crystal Structure Solution, University of Göttingen* **1997**; b) G. M. Sheldrick, *Acta Crystallogr., Sect. A* **2008**, *64*, 112–122.
[29] G. M. Sheldrick, *SHELXL-97, Program for Crystal Structure Refinement, University of Göttingen* **1997**.
[30] P. van der Sluis, A. L. Spek, *Acta Crystallogr., Sect. A* **1990**, *46*, 194–201.
[31] a) A. L. Spek, *J. Appl. Crystallogr.* **2003**, *36*, 7–13; b) A. L. Spek, *Acta Crystallogr., Sect. A* **1990**, *46*, C34.
[32] I. J. Bruno, J. C. Cole, P. R. Edgington, M. Kessler, C. F. Macrae, P. McCabe, J. Pearson, R. Taylor, *Acta Crystallogr., Sect. B* **2002**, *58*, 389–397.

Received: October 26, 2010
Published Online: February 11, 2011

